# Single bubble rise in GaInSn in a horizontal magnetic field

Richter, T.; Keplinger, O.; Shevchenko, N.; Wondrak, T.; Eckert, K.; Eckert, S.; Odenbach, S.;

Originally published:

July 2018

**International Journal of Multiphase Flow 104(2018), 32-41**

DOI: https://doi.org/10.1016/j.ijmultiphaseflow.2018.03.012

Perma-Link to Publication Repository of HZDR:

https://www.hzdr.de/publications/Publ-25763

# Single bubble rise in GaInSn in a horizontal magnetic field

T. Richter[a,*], O. Keplinger[b], T. Wondrak[b], K. Eckert[b], S. Eckert[b], S. Odenbach[a]

[a] *Institute of Fluid Mechanics, Chair of Magnetofluiddynamics, Measuring and Automation Technology, Technische Universität Dresden, D-01069 Dresden, Germany*
*E-mail: Thomas.Richter6@tu-dresden.de*
[b] *Helmholtz-Zentrum Dresden-Rossendorf (HZDR), Institute of Fluid Dynamics, PO Box 510119, 01314 Dresden, Germany*

**Abstract**

The rise of single gas bubbles of moderate size (~ 5 mm) in a liquid metal was studied in a flat container filled with the eutectic alloy GaInSn. The bubble motion is affected by a homogeneous horizontal magnetic field which is perpendicular to the width side of the fluid container. Measurements of the bubble trajectory, bubble velocity and deformation were performed by means of a combination of ultrasound transit time technique and X-ray radiography. In the hydrodynamic case without a magnetic field, the bubbles show the typical zig-zag movement whose attenuation can be observed for sufficiently high magnetic fields of B > 270 mT. The bubble trajectory becomes straight at a field strength of about 500 mT. A damping of the zig-zag path does not result in case of small magnetic fields applied. In this parameter range, even an increase of the amplitude of the lateral path oscillation is observed. Furthermore, this study revealed a discontinuity in the bubble path, which is called as "initial path instability" on the basis of its occurrence in the early stage of the bubble rise shortly after the bubble injection. This instability is characterized by an extreme inclination of the ellipsoidal bubble which often leads to a bubble "somersault". This instability is suppressed by a sufficiently high enough magnetic field. The reason for this instability and the magnetic field effect thereon are qualitatively discussed.

*Keywords:* ultrasound transit time technique, X-ray radiography, single bubble, GaInSn, bubble trajectory, initial path instability

## 1. Introduction

Two-phase flows are widely used in chemical engineering and metallurgy, e.g. as bubble-driven plumes for stirring and homogenizing melts. The optimization and control of these processes requires precise knowledge about bubble sizes, trajectories, velocities and residence times. In water and other transparent liquids, the rise of bubbles has been comprehensively studied. A bubble performs a rectilinear motion as long as the Reynolds number (Re) is smaller than 280 (Saffman [1] and Hartunian and Sears [2]). When Re > 280 the motion turns into a zig-zag trajectory (Magnaudet and Eames [3]). Ellingson and Riso [4] showed that the planar zig-zag motion,

*Corresponding author

appearing after an initial acceleration phase, is finally transformed into a helical motion. These trajectories are correlated with the vortex structure in the wake of the bubble, characterized by the formation of pairs of hairpin vortices. The alternating shedding of these vortices causes the zig-zag rise (Kelley and Wu [5]) while the appearance of a helical vortex structure triggers the crossover to a spiral bubble trajectory (Lunde and Perkins [6]).

Brücker [7] investigated the path instabilities of the bubble in detail, especially the zig-zag motion. A hairpin vortex pair is generated at one side of the bubble when it passes a reversal point. The counter-rotating vortex filaments induce a velocity in the direction of the zig-zag motion according to Biot-Savart law, which leads to the bubble tilting (Schwarz and Fröhlich [8]). The bubble returns to a horizontal position at the subsequent reversal point when the vorticity and the induced velocity diminish. The subsequent vortices are generated at the opposite side of the bubble. When the zig-zag trajectory shows a lateral drift, Brücker [7] presumes that a net lift force is acting on one vortex pair, which is weaker, and the zig-zag trajectory drifts in this direction. He also correlated wake structures with oscillations in the path and shape of the bubble. The shape oscillations result in a pair of counterrotating streamwise vortices within the near wake of the bubble [7].

Mougin and Magnaudet [9] and Shew et al. [10] analyzed the vortical forces $F_{\omega \mathrm{x}}$ and $F_{\omega \mathrm{y}}$ and the vortical torque $\Gamma_{\omega}$ acting on a bubble rising along a zig-zag path; these parameters are considered to be responsible for evoking the helical motion. The authors showed that $F_{\omega \mathrm{y}}$ determines the maximum inclination angle of the path and the bubble rotation rate.

Magnetic fields have the potential to influence the bubble motion in electrically conducting fluids. Although a direct effect on the non-conducting gas bubble can be excluded, a DC magnetic field acts on the surrounding liquid and, for example, dampens the fluid flow and changes the vortex structure in the bubble wake. For a recent review of relevant phenomena arising from an application of magnetic fields in liquid metals we refer to Fröhlich et al. [11]. Zhang et al. [12] investigated the rise of single Ar bubbles in GaInSn exposed to a vertical magnetic field. Among other things, they observed a straightening of the bubble path accompanied by first an increase and later a decrease in velocity for bigger bubbles when a vertical magnetic field up to B = 0.3 T is applied. Similar findings were reported by Wang et al. [13] for the case of a horizontally aligned magnetic field. For small magnetic fields (N < 1) the terminal velocity was increased for bubbles of an equivalent diameter of $d \geq 4.6$ mm whereas the application of higher magnetic fields reduces the bubble velocity.

Simulations of single bubbles rising in liquid metals under the influence of a vertical magnetic field were performed by Schwarz and Fröhlich [8] and Zhang and Ni [14]. Schwarz and Fröhlich described the damping of the vortical structures by a vertical magnetic field as follows: smaller structures vanish as the interaction parameter, N, increases and the larger vortex filaments become more closely aligned with the magnetic field. Zhang and Ni [14] also found an alignment of the vortex filaments and predicted a so-called "secondary path instability" for the bubble rise at interaction parameters slightly exceeding the value of 1 (N = 1.5 . . . N = 2.4). This "secondary path instability" is manifested by the fact that the magnetic field causes a disturbance in the rectilinear bubble path, although the straightening of the bubble trajectory was already achieved at slightly lower field intensities. As yet there is no experimental proof of this numerical finding. A further increase of the magnetic fields to significantly higher values of the magnetic interaction parameter N = 65 results again in a stable and straight bubble trajectory. By numerical simulations for a horizontal magnetic field, Zhang, Ni and Moreau [15] obtained a suppression of bubble velocity fluctuations for magnetic interaction parameters that clearly exceed the value of one. While small magnetic fields attenuate the small-scale vortices in the bubble wake, the

vorticity becomes almost perfectly aligned with the magnetic field direction for N ≈ 1, leading to a fairly stable wake. The "secondary path instability" was not observed in case of a horizontal magnetic field. The horizontal orientation of the magnetic field leads to a non-uniform effect on the bubble in the horizontal plane. Jin et al. [16] observed that the structure of the hairpin vortices in the bubble wake are rather complex for magnetic fields smaller than B ≤ 0.2 T. For larger fields, the flow structure appears to be more ordered, but, the vortices in the direction of the magnetic field are wider than those in opposite direction. For B = 0.5 T, it was observed that the wake structures are damped due to the Lorentz force and the bubble rises in a straight trajectory.

Experimental investigations of liquid metal two-phase flows require suitable measurement methods, but, only a few experimental techniques are available which deliver reliable data about the bubble behavior in opaque liquids. X-ray radiography can visualize the bubble rise (Iguchi et al. [17], Wang et al. [18], Shevchenko et al. [19]), but is limited to flat sample volumes due to X-ray absorption of the liquid metal. The ultrasound Doppler velocimetry (UDV) is particularly suited to determine flow structures in non-transparent fluids (Takeda [20], Eckert et al. [21]). For single bubble regimes and two-phase flows at low void fractions, UDV enables simultaneous measurements of both the liquid flow and the bubble velocity [12]). The ultrasound transit time technique (UTTT) is attractive for studying the bubble distribution or the contour dynamics of bubble plumes (Andruszkiewicz et al. [22]). Vogt et al. [23] combined the capabilities of UDV and UTTT to study the flow structures and the bubble distribution of a bubble plume interacting with a flow driven by a rotating magnetic field.

The objective of this work is to systematically study the rise of a single argon bubble in GaInSn in a *horizontal* magnetic field by means of UTTT. The special focus is on measuring the bubble's trajectory and horizontal velocity as a function of the applied magnetic field. For the case without a magnetic field, the UTTT data were compared to X-ray radiographic measurements of the bubble properties. As a result, measurement data are provided for the less studied case of the bubble rise in a horizontal field which can also serve as a basis for the validation of numerical simulations.

## 2. Experimental setup

Fig. 1 shows the experimental setup used within this study. An open vessel made of acrylic glass (wall thickness: 2.0 mm) with an inner rectangular cross section of 144 mm × 12 mm was filled up to a height of 144 mm with GaInSn, selected material data on which are collected in Table 1. All experiments were carried out at room temperature.

Table 1: Data of GaInSn at $\vartheta$ = 20°C [24, 25]

| $\rho$ [kg/m$^3$] | $\eta$ [mPas] | $\sigma$ [N/m] | $c$ [m/s] | $\sigma_{\mathrm{el}}$ [$\Omega^{-1}$cm$^{-1}$] |
|---|---|---|---|---|
| 6360 | 2.18 | $533 \cdot 10^{-3}$ | 2730 | 32900 |

A sharp injection needle, made of stainless steel, with an inner diameter of 0.785 mm was used as an orifice. The top of this needle was sharpened at an angle of 15°, which caused the bubble to detach in a preferred direction. The needle was placed in the center of the vessel, 7 mm above the bottom (Fig. 1 a), and adjusted such that the zig-zag motion took place in a plane parallel to the wide side of the vessel. Argon was injected into the liquid through this orifice with a sufficiently small flow rate of $Q_g$ = 0.011 cm$^3$/s which guaranteed a single bubble regime. The diameters

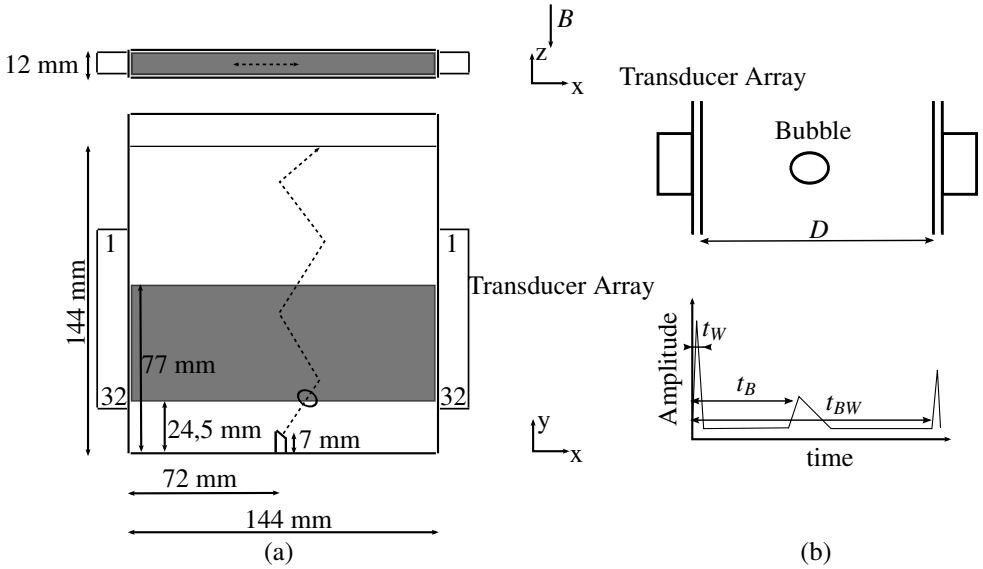


Figure 1: (a) Schematic diagram of the experimental setup from top and side view. The gray boxes indicate the measurement area. (b) Schematic drawing illustrating all parameters necessary for the data extraction, such as the inner dimension of the fluid vessel $D$ and the transit times $t_W$, $t_B$ and $t_{BW}$.

of the bubbles achieved with this setup were recently characterized in Richter et al. [26]: their equivalent diameter is $d_e = 5.22$ mm and the aspect ratio, given by the ratio of the major to the minor axis of the bubble, amounts to $a_r = 1.3$. Hence we are faced with elliptical bubbles (see Clift et al. [27]). Our aspect ratio is different from the $a_r = 3.6$ used in the simulations carried out by Zhang et al [15], and is also smaller than that in Jin et al. [16] who had an $a_r = 1.38$ and $a_r = 2.63$, respectively.

The horizontal magnetic field was generated by means of a DC electromagnet, the magnetic field ($B$) of which can be varied from 0 to 505 mT. The vessel was positioned such that the magnetic field was directed perpendicularly to the wide side of the vessel.

The UTTT transducer arrays, containing 32 elements 2.5 mm $\times$ 5 mm in size, were placed facing each other at the narrow side walls of the vessel, cf. Fig. 1 a. The measuring domain starts at a height of 24.5 mm and ends 77 mm above the vessel ground. The width of the measuring volume is approximately 6 mm.

The measuring principle of UTTT is based on single ultrasonic impulses emitted with a pulse repetition frequency $f_p$ by a transducer and is described in detail in [22]. The main information that is acquired is the distance between the position of the bubble surface facing the transducer and the transducer in discrete time steps $t_{meas}$, given in terms of multiples of the sampling time. This distance follows from:

$$x_B = c \cdot \frac{t_B - t_W}{2} \tag{1}$$

where $c$ is the sound velocity, $t_B$ the transit time from the transducer to the bubble surface and $t_W$

the transit time to pass the wall (illustrated in Fig. 1 b). The sound velocity can be expressed by:

$$c = \frac{2 \cdot D}{t_{BW} - t_W} \tag{2}$$

where $D$ is the inner size of the fluid vessel and $t_{BW}$ the transit time to the back wall. Eq. 1 combined with Eq. 2 leads to:

$$x_B = D \cdot \frac{t_B - t_W}{t_{BW} - t_W} \, . \tag{3}$$

The horizontal velocity $u_h$ can be obtained from the distance between subsequent bubble positions multiplied by the pulse repetition frequency:

$$u_h = (x_{Bi+1} - x_{Bi}) \cdot f_p \, . \tag{4}$$

The terminal vertical velocity of the bubble rise $u_v$ can be estimated by:

$$u_v = \frac{L}{\tau^*} \tag{5}$$

where $L$ describes the distance between two subsequent transducers and $\tau^*$ the time shift between their bubble signals. For a bubble rising in water Richter et al. [28] obtained a $u_v$, which agreed well with the validated on equation for bubbles rising in liquids [29].
The bubble diameter can be calculated by combining the signals of transducer arrays (subscripts i and j) placed at the same height level thus:

$$d_B = D \cdot \left(1 - \frac{t_{Bi} - t_{Wi}}{t_{BWi} - t_{Wi}} - \frac{t_{Bj} - t_{Wj}}{t_{BWj} - t_{Wj}}\right) \, . \tag{6}$$

The measured bubble surface shows fluctuations due to the effect of the bubble entering and exiting the ultrasound beam, as shown in [26]. To reconstruct the trajectory of the bubble's center of mass, we can calculate $x_{Bc}$ as follows:

$$x_{Bc} = x_B + \frac{d_B}{2} \, . \tag{7}$$

For more details we refer to Richter et al. [28], in which the error of the method was specified at 7%.
To characterize the bubble size, we introduce the equivalent bubble diameter, $d_e$, assuming a spherical bubble shape:

$$d_e = \left(V \cdot \frac{6}{\pi}\right)^{\frac{1}{3}} \, . \tag{8}$$

where V is the gas volume of the bubble.
As non-dimensional parameters for classifying the magnetic field effects on the bubble dynamics, we introduce the Hartmann number, $\mathrm{Ha} = B \cdot d_e \sqrt{\sigma_{el}/\eta}$, the magnetic interaction parameter, $\mathrm{N} = \frac{\sigma_{el} \cdot B^2 \, d_e}{\rho_l \cdot u}$, where $u$ is the terminal rising velocity of the bubble, and the Eötvös number $\mathrm{Eo} = (\rho_l - \rho_g) \cdot g \cdot d_e^2/\sigma$. In our study, the mean bubble diameter of $d_e = 5.22$ mm results in an Eötvös number $\mathrm{Eo} = 2.9$.

*X-ray setup.* A commercially available X-ray tube (GE ISOVOLT 450KV) produces a continuous conical polychromatic X-ray beam that penetrates the liquid metal along the narrow extension of the container. The non-absorbed part of the beam hits on a scintillation screen that is attached to the surface of the container. Its intensity is converted into a visible light distribution that is further deflected by a mirror and projected by a lens system on to a sensor plane of the sCMOS camera (pco.edge 5.5). The field of view was chosen to achieve the highest frame rate possible and was 75 mm × 120 mm at 130 frames per second. A short exposure time of 3 ms per image was adjusted to avoid blurring depiction of the quickly ascending bubbles. The image sequences were analyzed using Matlab codes to extract the bubble size, shape, orientation, velocity and trajectory. A more detailed description of the experimental setup can be found e.g. (Shevchenko et al. [19], Timmel et al. [30] and Vogt et al. [31]).

## 3. Results

The experimental configuration with respect to the orifice and the vessel geometry (see Fig. 1 a) promotes a planar zig-zag of the bubble parallel to the wide side of the vessel. The bubble rise under the influence of a magnetic field was investigated by UTTT for the full range of magnetic field values available ($0 \leq B \leq 505$ mT), while the X-ray measurements served to characterize the reference case for $B = 0$.

### *3.1. Bubble trajectory*

At least 20 bubbles were included in the analysis for each strength of the applied magnetic field. Only those bubbles were evaluated which were detected by all 5 transducer pairs. All evaluated bubbles displayed similar behavior: the bubbles rose along a zig-zag trajectory with a discontinuity on the path between the orifice and the first reversal point.

Fig. 2 shows the measured trajectories of one representative bubble with different magnetic fields expressed by the distance between transducer and bubble surface $x_B$ vs. the height $y$. The height $y$ was calculated from the product of the time step and the estimated vertical bubble velocity $u_v$ (Eq. 5). The green and blue lines show the measured outermost positions of the left and right bubble surfaces $x_B$ (Eq. 3), respectively, closest to the respective transducer, interpolated by the spline fits. The deduced center of mass of the bubble $x_{Bc}$ (Eq. 7) is indicated by red dots (the thick red line). This line is repeatedly interrupted by gaps caused by the bubble temporary disappearing out of the ultrasound cone of the respective transducers. The thin red line shows the interpolated spline fit of the bubble path filling these gaps.

When no magnetic field is applied, the bubbles perform a zig-zag rise with a period of approximately $T = 0.157 \pm 0.003$ s or, translated into a spatial wavelength by multiplying with $u_v$, of about 40 mm. The zig-zag motion is superimposed by a lateral drift in the zig-zag plane. This drift vanishes beyond a critical value of the magnetic field, as will be shown later. The reversal points of the zig-zag trajectory are marked by $RP_i$. The application of a sufficiently strong magnetic field ($B > 200$ mT) results in a remarkable damping of the zig-zag motion. The bubble rises on a straight path at $B = 505$ mT. On the way from orifice to the first reversal point $RP_1$ a discontinuity appears in the path of the bubble center. This exceptional behavior was reproducibly observed for every bubble. It is remarkable that this kink in the curve reliably disappears when a moderate magnetic field ($B > 148$ mT) is applied. This fact suggests that this phenomenon could be related to an instability. Because it is a robust phenomenon which has not been reported before in the literature and since it occurs before the first reversal point $RP_1$

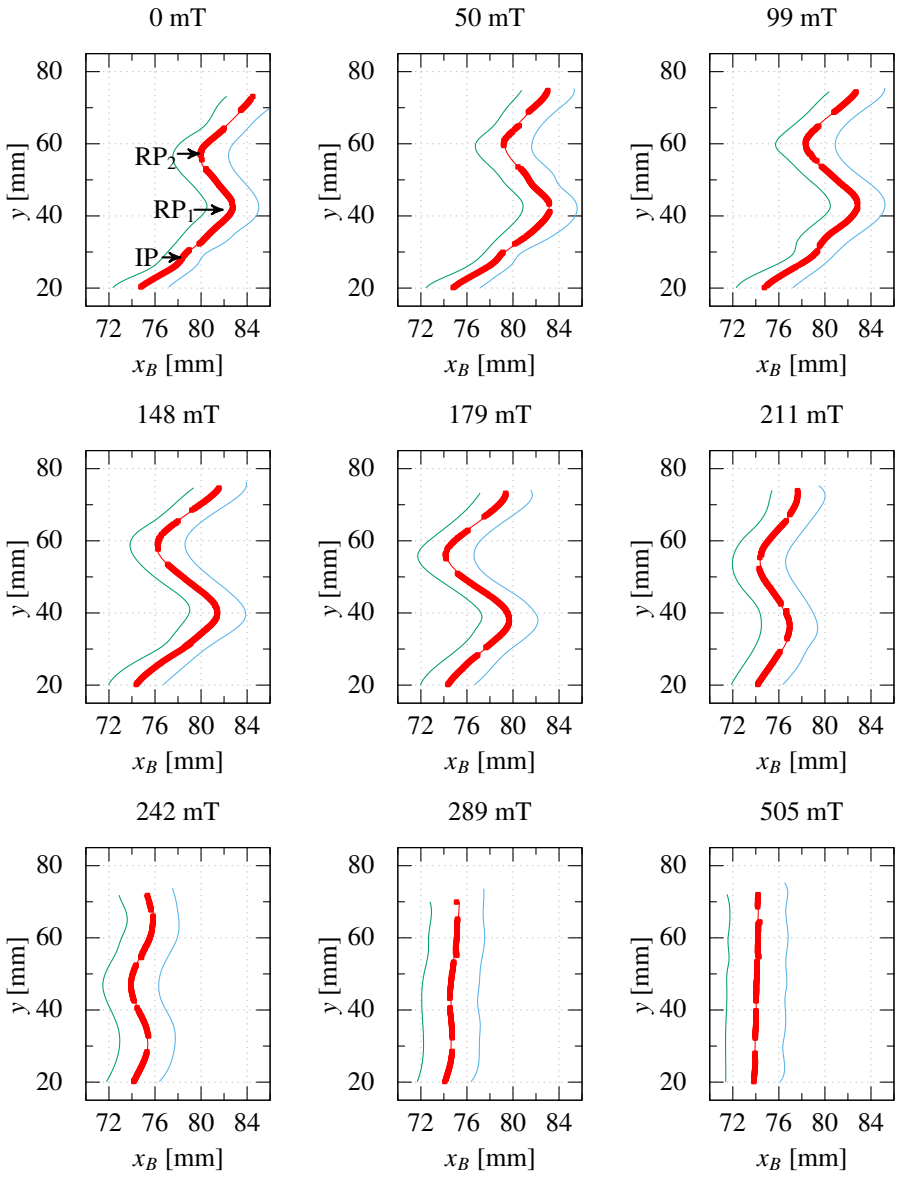


Figure 2: Bubble trajectory of a single bubble with different magnetic fields applied (0 - 505 mT). The red dots (lines) indicate the measured bubble position of the center of mass ($x_{Bc}$), the thin red lines the spline fit of the bubble path and blue and green lines the fit of the bubble surface position ($x_B$).

we refer to this phenomenon as an initial path instability. We mark this point by IP in Figs. 2, 3 and 4 b.

To characterize this initial path instability we plot the height $y$ of the bubble over the $x$-position and the horizontal velocity $u_h$ of the bubble, in Fig. 3 a as an example for $B = 99$ mT. It be-

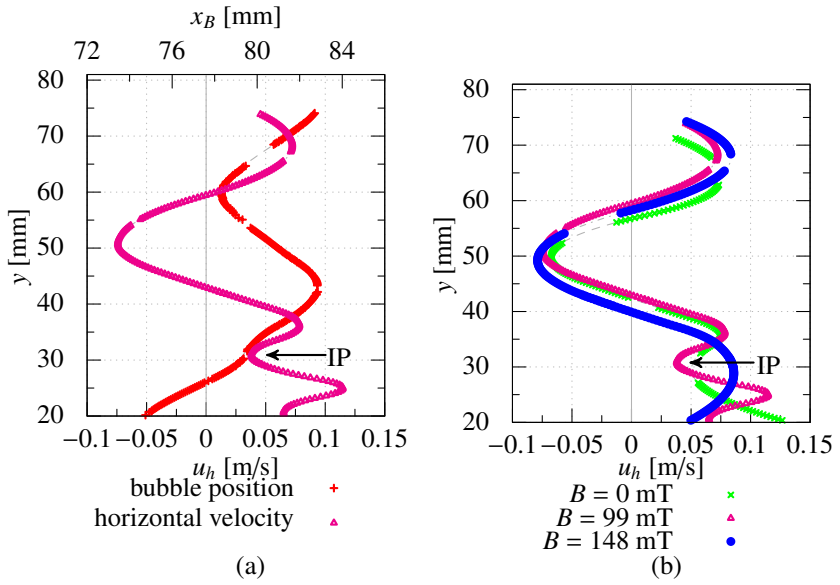


Figure 3: (a) Bubble position $x_b$ and the derived horizontal velocity $u_h$ of a bubble at $B = 99$ mT. Note the local minimum of $u_h$ at the initial path instability. (b) A comparison of $u_h$ of bubbles rising at different B shows that this local minimum vanishes as B increases.

comes apparent that the horizontal bubble velocity at the position of IP passes a local minimum before the first reversal point is reached. Thus, the bubble slows down during its approach to IP and again undergoes acceleration after passing IP. Fig. 3 b shows the horizontal velocity $u_h$ at three different magnitudes of B. The bubble rising without an applied magnetic field exhibits the largest $u_h$ at $y = 20$ mm, so we can assume that it undergoes strong acceleration just after detachment from th injection nozzle and reaches a local maximum of $u_h$ before it enters the measuring domain covered by the ultrasonic array. For a better understanding of this, we refer to Section 3.2. The local maximum of $u_h$ is reached at around $y \sim 25$ mm for $B = 99$ mT. This local maximum shifts its vertical position as the value of $B$ increases. The local minimum in $u_h$, which characterizes the initial path instability, disappears at a critical value of $B = 115$ mT. The initial path instability is further discussed in Section 3.2.

Figs. 4 and 5 analyze the shift in the positions of the $RP_i$ and IP as a function of the magnetic flux density. Fig. 4 a shows the vertical positions of the reversal points $RP_i$ and the initial path instability IP. These are extracted from interpolated spline fits of the bubble paths and averaged over the different measurements. The error bars refer to the standard deviation. For lower magnetic field values, the third reversal point $RP_3$ lays out of the sensing area, so it could not be detected in every measurement. With increasing $B$, which causes a downwards movement of the $RP_i$ into the measurement area, it is possible to reliably identify the $RP_3$ , see Fig. 4 a. The measurements show that the positions of the reversal points depend on the strength of the magnetic field, while the path instability occurs at approximately the same position.

Looking at the bubble path in the case without a magnetic field, it is noticeable that the vertical distance between the positions of the IP and $RP_1$ approximately equals the distance between subsequent reversal points. With disappearing of IP, which is detectable up to $B \approx 125$ mT, the

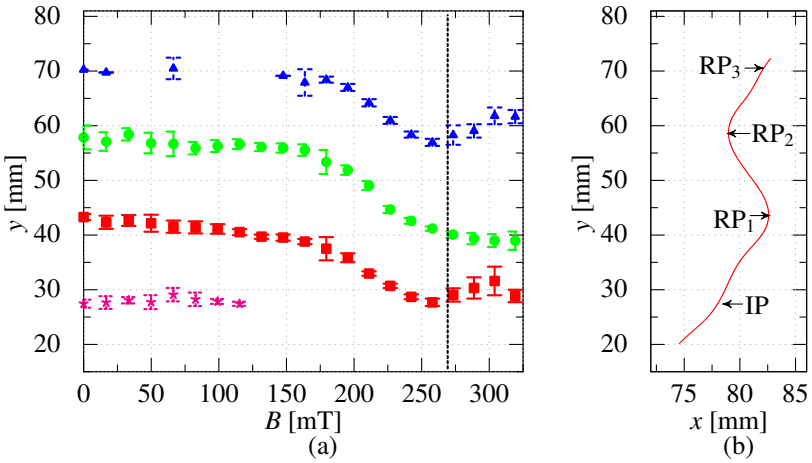


Figure 4: (a) Vertical position of the initial path instability (IP) and reversal points ($RP_i$) for different magnetic fields. The vertical line at $B$ = 270 mT marks the region until which a reliable detection of the positions of the reversal points is still possible. Please note that the key for this figure is identical with the one for Fig. 5. (b) Spline fit of a bubble trajectory, which visualizes the position of IP and the $RP_i$.

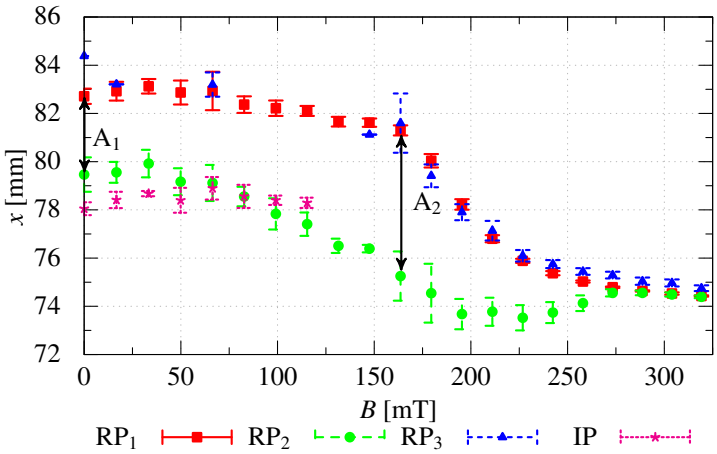


Figure 5: Horizontal position of the initial path instability (IP) and reversal points ($RP_i$) for different magnetic fields. The position of the nozzle is at $x$ = 72 mm.

application of an increasing magnetic field causes a continuous shift in the reversal points toward deeper positions in the fluid vessel. At a magnetic field strength of approx. 270 mT, $RP_1$ has reached the original vertical location of the IP. At the same time, the magnetic field attenuates the lateral dimension of the bubble trajectory, so that a determination of the reversal points for $B > 270$ mT is associated with an increasingly large measurement error. For a $B \leq 300$ mT, the bubble path becomes rectilinear, and the $RP_i$ are no longer detectable.

The horizontal coordinates of the $RP_i$ shown in Fig. 5 also mark the envelope of the bubble path. Fig. 5 shows clearly that the lateral positions of $RP_1$ and $RP_3$, as well as the positions of $RP_2$ and IP, coincide very well. An increasing magnetic field suppresses the lateral bubble motion,

leading to a reduction in the lateral distance of all $RP_i$s and IPs with respect to the $x$-coordinate of the orifice. It is interesting to note that the horizontal distance of $RP_1$ and $RP_2$ does not decrease continuously with growing magnetic field, but even increases before the lateral deflections are significantly attenuated (cf. Fig. 5 $A_1$ and $A_2$). This is caused by the stronger initial movement of $RP_2$ towards the $x$-position of the orifice, while $RP_1$ remains nearly at the same horizontal position. For $B = 273$ mT the trajectory is then nearly straight and the $x$-position of all reversal points coincide (approx 74 mm). The lateral drift is reduced when a magnetic field is applied and also vanishes after $B = 165$ mT. It appears that the approach of the successive $RP_i$ accelerates in a range of 115 mT $< B <$ 165 mT after IP is no longer detectable.

### *3.2. Bubble movement visualized by X-ray radiography*

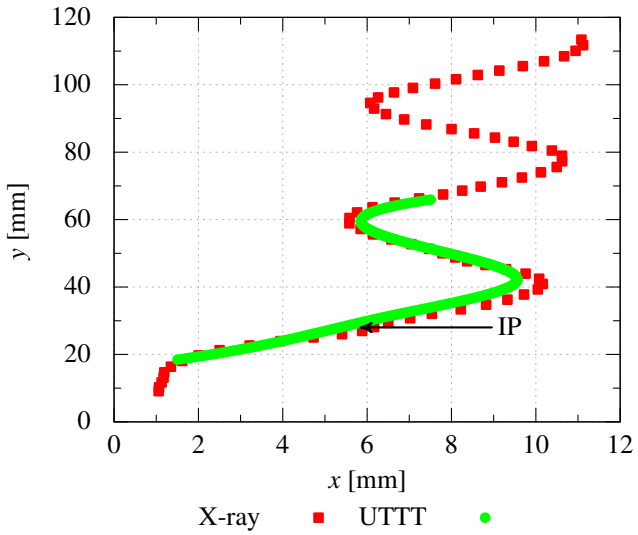


Figure 6: Comparison of bubble trajectories measured using UTTT and X-ray

A couple of experiments were performed for visualizing the behavior of the bubbles by means of X-ray radiography. These measurements had to be restricted to case B = 0 because the current experimental setup in the X-ray lab does not facilitate the integration of the magnetic system. To prove the value of the X-ray data for the interpretation of the UTTT data, Fig. 6 presents a comparison of the bubble trajectories measured using UTTT and X-ray radiography. The good agreement between the measured trajectories provides a sound basis for the subsequent quantitative analysis of the initial path instability.

The main goal of the investigations in this section was to better understand what actually happens during the so-called initial path instability. Fig. 7 shows the rise of a single bubble illustrated by overlapping of images sampled at different time steps. The location of the major axis of the ellipsoidal bubble is plotted in Fig. 7 a at a high frame rate ($\Delta t = 0.007$ s). The bubble contours are fitted by ellipsoids, shown for every third image ($\Delta t = 0.021$ s between neighboring ellipsoids) in Fig. 7 b. Fig. 7 c shows four pictures at the height of the initial path instability, IP ($z = 28$ mm). These figures reveal a distinct change in the orientation of the major axis of the bubble when the path instability occurs. This is observable in Fig. 7 a in the rotation of

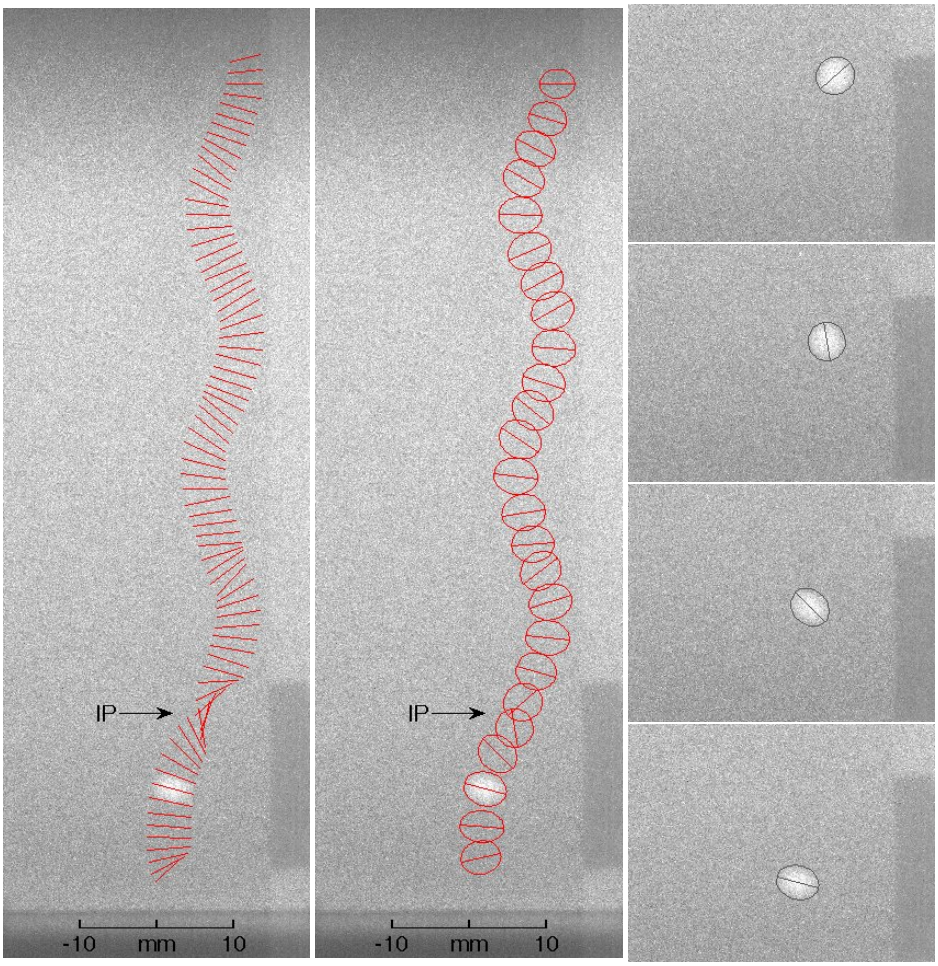


(a) (b) (c)

Figure 7: (a) Single bubble rise expressed by the location of the major axis at different time steps. (b) Single bubble rise (every third picture): the bubble shape is fitted by ellipsoids and the major axis, indicating the tilt, is shown. (c) Individual pictures of the rising bubble with fitted ellipsoidal shape at the height of the initial path instability. The bubble in this figure shows the "somersault" mode of the initial path instability.

the major axis, or in Fig. 7 b as a strong change in the tilt of the ellipsoid. All in all, the pictures show that the bubble performs a "somersault". This phenomenon has been found for about 70% of all bubble ascents visualized within this study. In the other cases, a spontaneous rebound of the extreme inclination of the bubble axis was observed.

Fig. 8 a shows the horizontal component $u_h$ and Fig. 8 b the vertical component $u_v$ of the bubble's velocity. We can see for $u_v$ that the bubble underwent strong initial acceleration and the velocity reached the maximum value before the IP. At every $RP_i$ the $u_v$ had a local extremum and $u_h$ became zero.

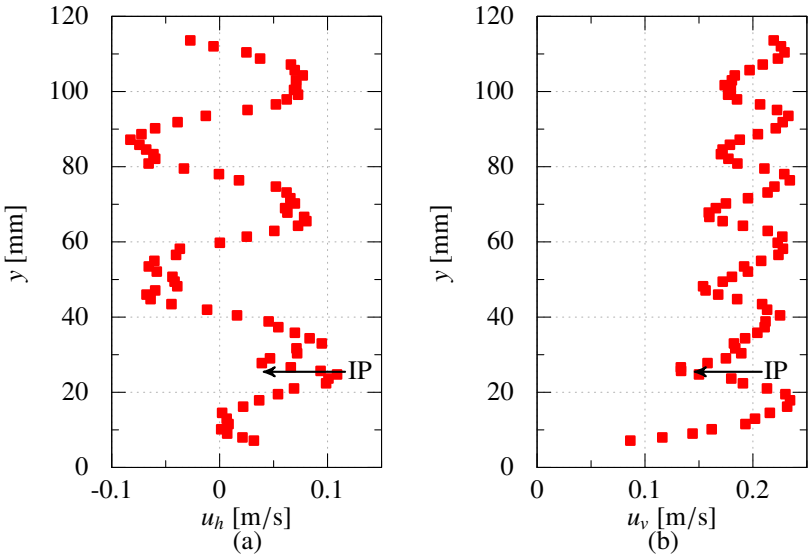


Figure 8: X-ray radiography: bubble velocity measured as a function of the height $y$: (a) horizontal component $u_h$ (b) vertical component $u_v$.

Figs. 9 and 10 visualize the two modes of the IP: Fig. 9 shows the "somersault" behavior and Fig. 10 the rebound of the bubble tilt. In each figure, (a) depicts the aspect ratio $a_r$ of the bubble, defined as the ratio of the major to the minor axis; in (b) the tilt angle of the major axis of the bubble is plotted. We discuss the bubble motion in two intervals. The first describes the bubble rise from the injection to the initial path instability and the second the rise of the bubble after IP. After injection, the bubble started with a small deformation ($a_r = 1.1$) which became rapidly more pronounced and reached a maximum aspect ratio of $a_r = 1.39$ at a height of about 12 mm above the vessel bottom. Afterwards, the bubble quickly returned to an almost spherical shape represented by a minimum aspect ratio of $a_r = 1.03$ at the IP. The bubble inclination for the same height started from a small negative value to a strong positive tilt. It is interesting to note that the zero inclination (horizontal alignment of the larger bubble axis) matched with the largest $a_r$. The bubble experienced strong acceleration after its injection up to a $u_v = 0.24$ m/s and afterwards a strong deceleration, meaning that $u_v$ decreased to a value smaller than 0.15 m/s. At the height of the largest aspect ratio $a_r$, $u_h$ became zero, then increased again before reaching a local minimum at IP. The strong deformation and the shift in the inclination of the bubble shortly after injection were caused by the bubble detachment from the orifice, which led to an initial oscillation in its shape (Longuet-Higgins et al. [32] and Oguz and Prosperetti [33]). Sanada et al. showed that there is an extension of the bubble prior to the detachment, leading to an oscillation afterwards [34]. This first extension and the subsequent oscillation causes the observed change in the deformation and tilt.

At the height of the initial path instability, the bubble revealed a strong tilt, accompanied by a reduction in the deformation and a low velocity. Later on, two types of movement were observed. The inclination flipped for the first case to a high negative value, which leads to the assumption that the bubble performed a "somersault", cf. Fig. 9 b. The rising velocity and the inclination increased again after the IP. After some delay, the bubble retained its nearly spherical shape al-

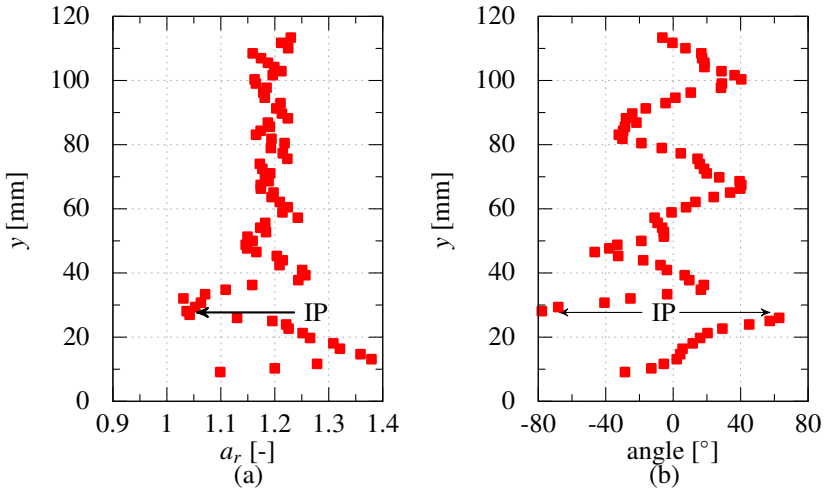


Figure 9: (a) Aspect ratio, $a_r$ (ratio of the major to minor axis of the ellipsoid) and (b) inclination of the major axis during the bubble rise. "Somersault" mode of the initial path instability.

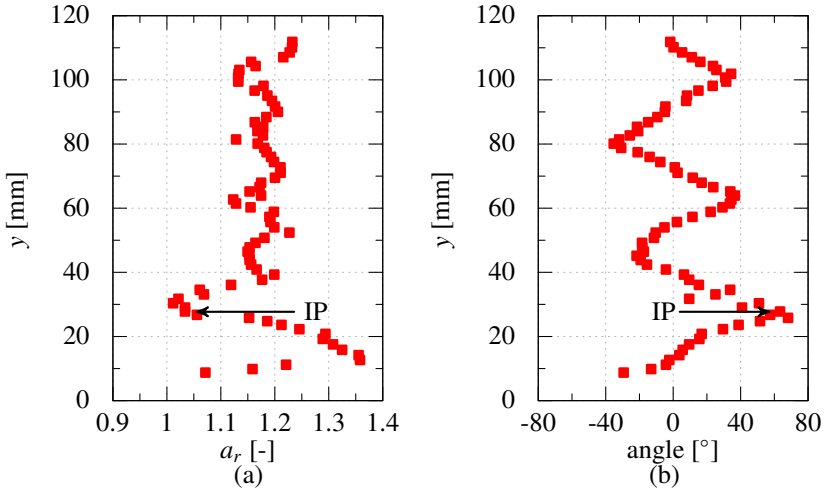


Figure 10: (a) Aspect ratio, $a_r$ (ratio of the major to minor axis of the ellipsoid) and (b) inclination of the major axis during the bubble rise for a single bubble. Spontaneous rebound mode of the initial path instability: visualization of the strong tilt and the subsequent turning back.

though its inclination changed. For the second case, the bubble's inclination decreased again after the strong tilt at IP, cf. Fig. 10 b, and its shape stayed nearly spherical, as in the first case. After the first reversal point, the bubble showed a planar zig-zag path, its major axis being positioned horizontally when the bubble passed a reversal point while a distinct bubble tilt appears on the way to the next reversal point. The bubble had a maximum inclination of around 40° and the deformation fluctuated around $a_r = 1.2$ during the rise. The horizontal velocity $u_h$ alternated between -0.08 and 0.08 m/s and changed its sign at the reversal points. The vertical component $u_v$ reached maximum values at the height of the reversal points and minimum values in between,

with a slightly increasing mean velocity.
This strong tilt and the nearly spherical shape at the height of IP explains the perturbation of the bubble path which was detected by UTTT.

## 4. Discussion

This work presents an experimental investigation of the planar zig-zag rise of argon bubbles in a liquid metal under the influence of a horizontal magnetic field. The measurements revealed an anomaly in the bubble trajectory which was named as the *initial path instability*. As mentioned before, the zig-zag motion is caused by the pairwise shedding of hairpin vortices. The counter-rotating vortex filaments induce a horizontal velocity component leading to the zig-zag motion and the tilting of the bubble. The bubble returns to a horizontal position, when the vorticity and the induced velocity decay. The next generation of vortices appears at the opposite side of the bubble [8, 7].
The damping of the vortex structures by a vertical magnetic field was described by Davidson [35]: small-scale structures of the isotropic turbulence are effectively dissipated by Joule heating whereas larger vortex filaments are not affected by Joule dissipation provided their axes are aligned with the magnetic field. Such a behavior was reported for a bubble rise in a horizontal magnetic field based on numerical simulations [8, 14]. For small N, smaller vortex structures vanish and the hairpin vortices in the direction of the magnetic field are wider than those in the opposite direction [16]. With increasing N, the vorticity becomes aligned in vertical direction [15].
A particularly interesting feature is the observed initial path instability (IP), which was not reported in the literature on liquid metal two-phase flows so far. This instability was also not observed for single bubbles rising in water, either in our own work [28] or in those in the literature, see for example Tachibana and Saito [36]. We note that an elongated distance between the injection and first reversal point was also observed in their experiments, but no anomaly was seen in the bubble path. Obviously, the reason has to be sought in the significant differences in density and surface tension between GaInSn and water. Note that the density of GaInSn is six times greater than that of water. As a result, the initial acceleration of the bubble in the liquid metal is higher and inertial forces are stronger. The surface tension of GaInSn is about ten times that of water, hence, the forces restoring a spherical interface are also considerably stronger.
One characteristic feature of the IP is the occurrence of a very strong inclination in combination with a nearly spherical shape. The IP occurs independently of the magnetic field but it can be influenced by the latter up to the point of complete suppression. The horizontal and vertical positions of the initial path instability seem to fit those of the reversal points of the zig-zag trajectory. Thus, it is possible that this initial path instability point could be interpreted either as a misguided reversal point or as a delayed onset of the zig-zag. The diagram in Fig. 11 serves to illustrate the hypothesis on the origin of this behavior.

Let us assume that the first pair of hairpin vortices, just after detachment from the nozzle, has a larger vorticity and a stronger $F_\omega$ (Fig. 11 A). This stronger vorticity induces a higher horizontal velocity, which leads to the observed strong tilt and the stronger $F_\omega$ resulting in a larger inclination angle. The lateral velocity and tilt might be so strong that the bubble turns over. While it turns over, a slight decrease in the horizontal velocity (Fig. 3 b) and an almost spherical shape (Fig. 9 a) are observed. From this we can assume that the first vortex pair has detached. Afterwards, a second vortex pair might be generated at the same side of the bubble (Fig. 11 C) and the bubble moves on toward the first reversal point (Fig. 11 D). The horizontal

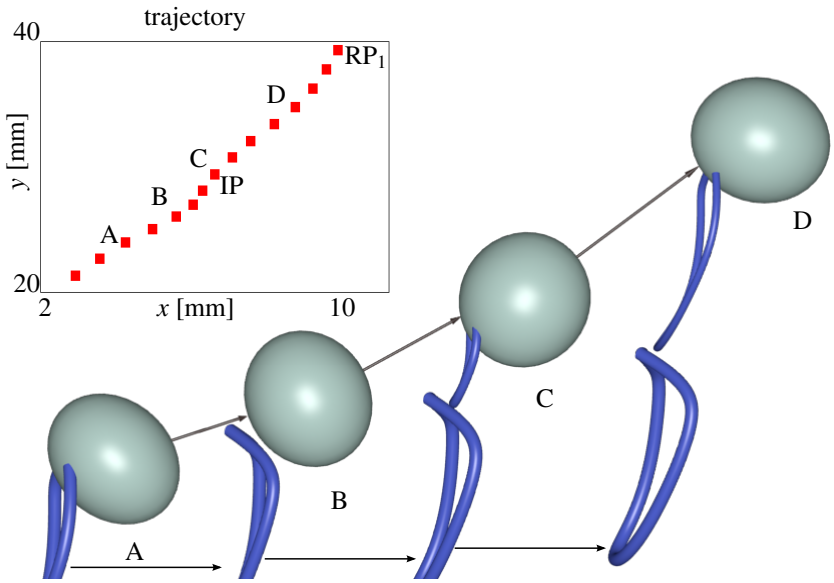


Figure 11: Schematic diagram of the bubble movement. The first strong hairpin vortex pair induces a strong horizontal velocity, which leads to the very strong tilt (A). The vortex pair detaches (B) and a new pair, weaker than the first one, is generated (C) and the bubble moves on to the first reversal point (D). The graph in the upper left corner visualizes a detail of the bubble rise.

velocity and the deformation increases slightly again. Thus, it seems that the second vortex pair might have a weaker vorticity compared to the first one.
After a critical value of N $\geq$ 0.21 ($B$ = 131 mT, Ha = 27) is reached, the initial path instability is no longer observable. Obviously, the induced horizontal velocity is no longer strong enough and it seems that the first vortex pair remains attached. With further increasing N $\geq$ 0.33 ($B$ = 163 mT, Ha = 34) the vertical position of the reversal points moves downwards (Fig. 4 a) which might cause a shortening of the first vortex pair. The induced horizontal velocity is attenuated by the Lorentz force, and the bubble path becomes nearly straight N = 0.86 ($B$ = 270 mT, Ha = 56).
The bubble detachment can also influence the generation of this strong first pair of hairpin vortices. An asymmetric detachment can lead e.g. to a lateral impulse and additional deformation of the bubble. Another point of importance is the interaction with the higher inertial and surface forces, caused by the high density and surface tension of the liquid metal.

## 5. Summary and conclusions

This work presents a systematic experimental study of a single bubble rising in GaInSn in a horizontal magnetic field. This bubble rise was investigated by means of UTTT and X-ray radiography. The bubbles performed a planar zig-zag motion with a lateral drift during the rise. When a horizontal magnetic field was applied, first the drift was suppressed and later the zig-zag

straightened until the bubble rose on a nearly straight path for B $\geq$ 270 mT. This transformation from a zig-zag rise to a straight path was investigated by tracking the movement of the reversal points of the zig-zag in vertical and horizontal directions. Furthermore, an initial path instability in this zig-zag trajectory was observed. Along with a deceleration of the bubble, the instability caused the ellipsoidal bubble to tilt strongly, up to a "somersault"-like movement with an intermediate, nearly spherical bubble shape.
The initial path instability vanished beyond a critical value of the applied magnetic field. A preliminary qualitative explanation of the instability is given taking into account the larger inertial and interfacial forces due to the high density and surface tension of GaInSn. We hope that this work will stimulate numerical studies to further elucidate the physical origin of these instabilities, which are obviously a special feature of bubbles rising in liquid metals.

## Acknowledgements

Financial support by the Helmholtz Alliance LIMTECH (project YIG) is gratefully acknowledged. We thank N. Shevchenko and E. Strumpf for their support of the measurements.

## References

[1] P. Saffman, On the rise of small air bubbles in water, Journal of Fluid Mechanics 1 (03) (1956) 249–275.
[2] R. A. Hartunian, W. Sears, On the instability of small gas bubbles moving uniformly in various liquids, Journal of Fluid Mechanics 3 (01) (1957) 27–47.
[3] J. Magnaudet, I. Eames, The motion of high-Reynolds-number bubbles in inhomogeneous flows, Annual Review of Fluid Mechanics 32 (1) (2000) 659–708.
[4] K. Ellingsen, F. Risso, On the rise of an ellipsoidal bubble in water: oscillatory paths and liquid-induced velocity, Journal of Fluid Mechanics 440 (2001) 235–268.
[5] E. Kelley, M. Wu, Path instabilities of rising air bubbles in a Hele-Shaw cell, Physical Review Letters 79 (7) (1997) 1265.
[6] K. Lunde, R. Perkins, Observations on wakes behind spheroidal bubbles and particles, in: ASME-FED Summer Meeting, Vancouver, Canada, Paper No. FEDSM97–3530, 1997.
[7] C. Brücker, Structure and dynamics of the wake of bubbles and its relevance for bubble interaction, Physics of Fluids (1994-present) 11 (7) (1999) 1781–1796.
[8] S. Schwarz, J. Fröhlich, Numerical study of single bubble motion in liquid metal exposed to a longitudinal magnetic field, International Journal of Multiphase Flow 62 (2014) 134–151.
[9] G. Mougin, J. Magnaudet, Wake-induced forces and torques on a zigzagging/spiralling bubble, Journal of Fluid Mechanics 567 (00) (2006) 185–194.
[10] W. L. Shew, S. Poncet, J.-F. Pinton, Force measurements on rising bubbles, Journal of Fluid Mechanics 569 (2006) 51.
[11] J. Fröhlich, S. Schwarz, S. Heitkam, C. Santarelli, C. Zhang, T. Vogt, S. Boden, A. Andruszkiewicz, K. Eckert, S. Odenbach, et al., Influence of magnetic fields on the behavior of bubbles in liquid metals, The European Physical Journal. Special topics 220 (2013) 167–183.
[12] C. Zhang, S. Eckert, G. Gerbeth, Experimental study of single bubble motion in a liquid metal column exposed to a DC magnetic field, International Journal of Multiphase Flow 31 (7) (2005) 824–842.
[13] Z. Wang, S. Wang, X. Meng, M. Ni, Udv measurements of single bubble rising in a liquid metal galinstan with a transverse magnetic field, International Journal of Multiphase Flow 94 (2017) 201–208.
[14] J. Zhang, M.-J. Ni, Direct simulation of single bubble motion under vertical magnetic field: Paths and wakes, Physics of Fluids (1994-present) 26 (10) (2014) 102102.
[15] J. Zhang, M.-J. Ni, R. Moreau, Rising motion of a single bubble through a liquid metal in the presence of a horizontal magnetic field, Physics of Fluids (1994-present) 28 (3) (2016) 032101.
[16] K. Jin, P. Kumar, S. Vanka, B. Thomas, Rise of an argon bubble in liquid steel in the presence of a transverse magnetic field, Physics of Fluids (1994-present) 28 (9) (2016) 093301.
[17] M. Iguchi, T. Chihara, N. Takanashi, Y. Ogawa, N. Tokumitsu, Z.-i. Morita, X-ray fluoroscopic observation of bubble characteristics in a molten iron bath, ISIJ international 35 (11) (1995) 1354–1361.

[18] Z. Wang, K. Mukai, D. Izu, Influence of wettability on the behavior of argon bubbles and fluid flow inside the nozzle and mold, ISIJ international 39 (2) (1999) 154–163.
[19] N. Shevchenko, S. Boden, S. Eckert, D. Borin, M. Heinze, S. Odenbach, Application of X-ray radioscopic methods for characterization of two-phase phenomena and solidification processes in metallic melts, The European Physical Journal Special Topics 220 (1) (2013) 63–77.
[20] Y. Takeda, Ultrasonic Doppler velocity profiler for fluid flow, Vol. 101, Springer, 2012.
[21] S. Eckert, G. Gerbeth, V. Melnikov, Velocity measurements at high temperatures by ultrasound Doppler velocimetry using an acoustic wave guide, Experiments in Fluids 35 (5) (2003) 381–388.
[22] A. Andruszkiewicz, K. Eckert, S. Eckert, S. Odenbach, Gas bubble detection in liquid metals by means of the ultrasound transit-time-technique, The European Physical Journal Special Topics 220 (1) (2013) 53–62.
[23] T. Vogt, A. Andruszkiewicz, S. Eckert, K. Eckert, S. Odenbach, G. Gerbeth, Mixing Enhancement in Gas-Stirred Melts by Rotating Magnetic Fields, Metallurgical and Materials Transactions B 43 (6) (2012) 1454–1464.
[24] N. Morley, J. Burris, L. Cadwallader, M. Nornberg, GaInSn usage in the research laboratory, Review of Scientific Instruments 79 (5) (2008) 056107.
[25] Y. Plevachuk, V. Sklyarchuk, S. Eckert, G. Gerbeth, R. Novakovic, Thermophysical properties of the liquid Ga–In–Sn eutectic alloy, Journal of Chemical & Engineering Data 59 (3) (2014) 757–763.
[26] T. Richter, O. Keplinger, E. Strumpf, T. Wondrak, K. Eckert, S. Eckert, S. Odenbach, Measurements of the diameter of rising gas bubbles by means of the ultrasound transit time technique, Magnetohydrodynamics 53 (2) (2017) 383–392.
[27] R. Clift, J. R. Grace, M. E. Weber, Bubbles, drops, and particles, Courier Corporation, 1978.
[28] T. Richter, K. Eckert, X. Yang, S. Odenbach, Measuring the diameter of rising gas bubbles by means of the ultrasound transit time technique, Nuclear Engineering and Design 291 (2015) 64–70.
[29] H. D. Mendelson, The prediction of bubble terminal velocities from wave theory, AIChE Journal 13 (2) (1967) 250–253.
[30] K. Timmel, N. Shevchenko, M. Röder, M. Anderhuber, P. Gardin, S. Eckert, G. Gerbeth, Visualization of liquid metal two-phase flows in a physical model of the continuous casting process of steel, Metallurgical and Materials Transactions B 46 (2) (2015) 700–710.
[31] T. Vogt, S. Boden, A. Andruszkiewicz, K. Eckert, S. Eckert, G. Gerbeth, Detection of gas entrainment into liquid metals, Nuclear Engineering and Design 294 (2015) 16–23.
[32] M. Longuet-Higgins, B. R. Kerman, K. Lunde, The release of air bubbles from an underwater nozzle, The Journal of the Acoustical Society of America 89 (4B) (1991) 2014–2014.
[33] H. N. Oguz, A. Prosperetti, Dynamics of bubble growth and detachment from a needle, Journal of Fluid Mechanics 257 (1993) 111–145.
[34] T. Sanada, M. Watanabe, T. Fukano, A. Kariyasaki, Behavior of a single coherent gas bubble chain and surrounding liquid jet flow structure, Chemical Engineering Science 60 (17) (2005) 4886–4900.
[35] P. Davidson, Magnetic damping of jets and vortices, Journal of Fluid Mechanics 299 (1995) 153–186.
[36] R. Tachibana, T. Saito, A Relationship Between the Motion of a Zigzagging Bubble and its Surrounding Liquid Motion, in: ASME-JSME-KSME 2011 Joint Fluids Engineering Conference, American Society of Mechanical Engineers, 2011, pp. 2693–2700.